

# Unraveling the Role and Impact of Alumina on the Nucleation and Reversibility of $\beta$ -LiAl in Aluminum Anode Based Lithium-Ion Batteries

Lucas Wells<sup>+, \* [a]</sup> Thien An Pham<sup>+, \* [b, c]</sup> Gebrekidan Gebresilassie Eshetu<sup>\*, [a, d]</sup>  
Stefan Seidlmayer<sup>[b]</sup> Giovanni Ceccio<sup>[e]</sup> Antonino Cannavo<sup>[f]</sup> Jiří Vacík<sup>[e]</sup> Adrian Mikitisin<sup>[g]</sup>  
Peter Müller-Buschbaum<sup>[c]</sup> Ralph Gilles<sup>[b]</sup> and Egbert Figgemeier<sup>\*, [a, h]</sup>

Aluminum, due to its high abundance, very attractive theoretical capacity, low cost, low (de-) lithiation potential, light weight, and effective suppression of dendrite growth, is considered as a promising anode candidate for lithium-ion batteries (LIBs). However, its practical application is hindered due to multiple detrimental challenges, including the formation of an amorphous surface oxide layer, pulverization, and insufficient lithium diffusion kinetics in the  $\alpha$ -phase. These outstanding intrinsic challenges need to be addressed to facilitate the commercial production of Al-based batteries. The native passivation layer,  $\text{Al}_2\text{O}_3$ , plays a critical role in the nucleation and reversibility of lithiating aluminum and is thoroughly investigated in this study using high precision

electrochemical micro calorimetry. The enthalpy of crystallization of  $\beta$ -LiAl is found to be  $40.5 \text{ kJ mol}^{-1}$ , which is in a strong agreement with the value obtained by calculation using Nernst equation ( $40.04 \text{ kJ mol}^{-1}$ ). Surface treatment of the active material by the addition of 25 nm of alumina increases the nucleation energy barrier by 83% over the native oxide layer. After the initial nucleation, the added alumina does not negatively impact the reversibility at 0.1 C rate, suggesting the removal of alumina is not necessary for improving the cyclability of aluminum anode based lithium-ion batteries. Moreover, the coulombic efficiencies are also found to be slightly higher in the alumina treated samples compared to the untreated ones.

## 1. Introduction

Anode materials involving alloying chemistry (e.g., Silicon, Aluminium, Tin etc.) are presented to be alluring alternatives to intercalation-type anodes (e.g., state-of-the-art and industry standard graphite). This is attributed to their unparalleled higher gravimetric and volumetric capacity. Among alloying anode materials, aluminum (Al) appears to be a highly attractive

anode candidate for lithium-ion batteries (LIBs) and this is due to its various beneficial features such as high abundance ( $2^{\text{nd}}$  most abundant metal), light weight, very attractive theoretical capacity (i.e., 993 mA/g, 1490 mAh/g and 2235 mAh/g for AlLi,  $\text{Al}_2\text{Li}_3$  and  $\text{Al}_4\text{Li}_9$  phases, respectively), relatively low cost ( $\sim \$2 \text{ kg}^{-1}$ ),<sup>[1]</sup> low and suitable (de-) lithiation potential ( $\sim 0.2$ – $0.45 \text{ V vs. Li}^+/\text{Li}$ ), effective suppression of dendrite growth, environmental benignity, and sustainability. Compared to most

[a] L. Wells,<sup>+</sup> G. G. Eshetu, E. Figgemeier  
ISEA Institut für Stromrichtertechnik und Elektrische Antriebe  
RWTH Aachen  
Campus-Boulevard 89, 52074 Aachen, Germany  
E-mail: Lucas.Wells@batt-ing.de  
Gebrekidan.Eshetu@isea.rwth-aachen.de  
Egbert.Figgemeier@isea.rwth-aachen.de

[b] T. A. Pham,<sup>+</sup> S. Seidlmayer, R. Gilles  
Heinz Maier-Leibnitz Zentrum  
Technical University of Munich  
Lichtenbergstraße 1, 85748 Garching, Germany  
E-mail: Thien-An.Pham@frm2.tum.de

[c] T. A. Pham,<sup>+</sup> P. Müller-Buschbaum  
TUM School of Natural Sciences, Department of Physics, Chair for  
Functional Materials  
Technical University of Munich  
James-Franck-Str. 1, 85748 Garching, Germany

[d] G. G. Eshetu  
Department of Material Science and Engineering  
Mekelle Institute of Technology, Mekelle University, P.O. Box 1632, Mekelle,  
Ethiopia


[e] G. Ceccio, J. Vacík  
Academy of Sciences of the Czech Republic  
Nuclear Physics Institute  
CZ-25068 Řež, Czech Republic


[f] A. Cannavo  
Collider Accelerator Department  
Brookhaven National Laboratory (BNL)  
Upton, NY-11973-5000, USA

[g] A. Mikitisin  
GFE Wissenschaftlicher Mitarbeiter  
being Gemeinschaftslabor für Elektronenmikroskopie RWTH Aachen  
Campus-Boulevard 89, 52074 Aachen, Germany

[h] E. Figgemeier  
Jülich Aachen Research Alliance, JARA-Energy  
52425 Jülich (Germany)

[<sup>+</sup>] L.W. and T.P. contributed equally to this work.

 Supporting information for this article is available on the WWW under  
<https://doi.org/10.1002/celec.202400322>

 © 2024 The Authors. ChemElectroChem published by Wiley-VCH GmbH. This is an open access article under the terms of the Creative Commons Attribution License, which permits use, distribution and reproduction in any medium, provided the original work is properly cited.

of the alloying anode materials, aluminum has a decidedly lower volume expansion upon (de-) alloying, i.e., 96% for  $\alpha$ -LiAl $\rightarrow\beta$ -LiAl compared to >280%/400% for Si to Li<sub>3.75</sub>Si/Li<sub>4.4</sub>Si, and 310% for Sn to Li<sub>22</sub>Sn<sub>5</sub>, and this leads to less mechanical stress and thus, pulverization of particles; and the loss of electrical contact between individual particles and the current collector during long-term cycling.<sup>[2]</sup>

However, despite the fact that Al was studied as a potential lithium storage material as early as 1970 s,<sup>[3]</sup> its practical application has not yet been fully realized. This originates from the presence of multiple inter-linked inherent challenges such as: 1) the formation of an amorphous surface oxide layer,<sup>[4]</sup> 2) a large difference in lithium diffusion kinetics between the  $\alpha$ - and  $\beta$ -LiAl phases (i.e.,  $10^{-8}$  to  $10^{-9}$  cm<sup>2</sup>s<sup>-1</sup> in  $\beta$ -LiAl, and  $\sim 10^{-11}$  cm<sup>2</sup>s<sup>-1</sup> in  $\alpha$ -LiAl),<sup>[5]</sup> which leads to diffusional lithium trapping,<sup>[6,7]</sup> 3) mechanical brittleness of the lithiated phases,<sup>[8]</sup> 4) heterogeneous nucleation with unequally distributed interfacial strain,<sup>[9,10]</sup> and 5) formation of nanopores/voids after  $\beta$ -to- $\alpha$ -phase transformation.<sup>[4,11,7]</sup> All result in accelerated capacity fading leading to low coulombic efficiency and poor long-term cycling stability. Moreover, due to synthesis related difficulty and extreme flammability of fine Al powders, it is found to be problematic to integrate Al into traditional slurry-coated electrode design and is the reason why there has been a growing interest on Al foil based anodes, which are also inexpensive and highly scalable.<sup>[1]</sup>

It is noteworthy to mention that in defiance of the monumental enthusiasm in navigating and researching new anode candidates, both by the academic and industries, Al has not relatively received the much deserved attention considering its intrinsic attractive properties that are essential for anode materials, for instance, compared to its silicon counterpart.<sup>[12]</sup>

Notable findings by Park et al. on anode material of carbon and aluminium hybrid nanoparticles (40 wt% AlC<sub>60</sub>) demonstrated to sustain a capacity of >900 mAh g<sup>-1</sup> for over 100 cycles.<sup>[13]</sup> To this day, there has been growing efforts by various researchers across the world to understand the working and failure mechanisms of aluminum anode - based lithium-ion batteries.<sup>[1,7,9,11,14]</sup>

Considering the huge potential of Al as anode materials for LIBs, there is a need for an in-depth investigation to holistically comprehend the root causes of the various failure mechanisms and their subsequent impact on the electrochemical performance.

Owing to its significant importance, this work focuses and investigates the mechanism towards the decisive role of alumina (Al<sub>2</sub>O<sub>3</sub>) in the nucleation and reversibility of  $\beta$ -LiAl production. To gain a deeper insight into the mechanistic understanding, several analytical tools including X-ray diffraction (XRD), high precision electrochemical micro calorimetry and neutron depth profiling (NDP) have been employed. Since recently, NDP has emerged as a recognized analytical technique for an in-depth understanding of Li-ion batteries, enabling the precise determination of a Li depth profile.<sup>[15,16,17]</sup>

The enthalpy of crystallization of  $\beta$ -LiAl, as determined by electrochemical micro calorimetry, is found to be 40.5 kJ mol<sup>-1</sup>, in a strong agreement with the value calculated using Nernst

equation (40.04 kJ mol<sup>-1</sup>). Surface treatment of Al (i.e., active material) by the addition of 25 nm of alumina is found to increase the nucleation energy barrier by 83% (222 vs. 121 kJ mol<sup>-1</sup>) over the native oxide layer. Moreover, surface treatment is found to slightly increase the coulombic efficiencies compared to untreated ones.

Finally, the systematic investigation approach implemented in this work presents to be of significant importance and will spur an out-of-box roadmap and direction to comprehensively understand and thus overcome the intrinsic challenges associated with Al anode and thereby facilitate the practical deployment of Al-anode based LIBs.

## Experimental

### Electrode and Coin Cell Preparation

2032 coin cell hardware and 200  $\mu$ m thick lithium chips were used (Gelion LIC Group, China). The working electrode was aluminum foil (cathode substrate) from MTI XTL. Wattman GF-C fiber paper was used as a separator and the electrolyte is a blend of ethylene carbonate (EC) and ethyl-methyl carbonate (EMC) in a 3 to 7 ratio by wt% with 1.2 M LiPF<sub>6</sub> as ion conducting salt and 10 wt% fluoroethylene carbonate (FEC) as an electrolyte additive. The cells were assembled in a dry room with a dew point below -55 °C. All hardware and electrodes were dried for 24 hours under vacuum at 80 °C before use. The cells were then sealed with an epoxy (Torr Seal, Agilent) to eliminate any noise from the heats of vaporization of electrolyte leaving the test samples.

### Materials and Material Processing

Scanning electron microscopy (SEM) with energy dispersive X-ray spectroscopy (EDX) was used to investigate the aluminum foil sample. Cross-section samples were prepared by argon ion polishing using an SM-09010 polisher by JEOL. The SEM measurements were performed using a SEminiSEM 300 (Carl Zeiss Microscopy). Secondary electron (SE) and backscattered electron (BSE) images were collected at 15 keV. Panoramic images were produced by using Atlas software V. 5.3.5.3 (Carl Zeiss Microscopy). EDX was performed using Ultimex 65 SDD-detector and Atec V. 6.0 software (Oxford Instruments) and it was operated at 15 keV and the spectra was collected at 10s live-time. The collection time of maps differed due to drift effects.

The working electrode tested is a readily available lithium-ion cathode substrate from MTI XTL (EQ-bcaf-15u-280). This foil is >99.3% aluminium with a thickness of 15  $\mu$ m thick (Figure 1a). While it is reported to be <0.3% iron, the authors of this study found that the cross sectioned images display micron sized iron throughout and a notable amount of iron on one side (Figure 1b). This is likely to emanate from a rolling process as the two sides also have visually different roughness. The side with less iron was oriented facing the counter electrode. The presence of an amorphous surface layer can be seen as a nodular growth on the surface and along grain boundaries in Figure 1c.

An additional test group consists of this foil that had been processed by Solaytec. Atomic layer deposition was used to deposit an additional 25 nm of alumina on the substrate. This is approximately ten times greater than the thickness of the native passivation layer. Care was taken to ensure that the deposition was

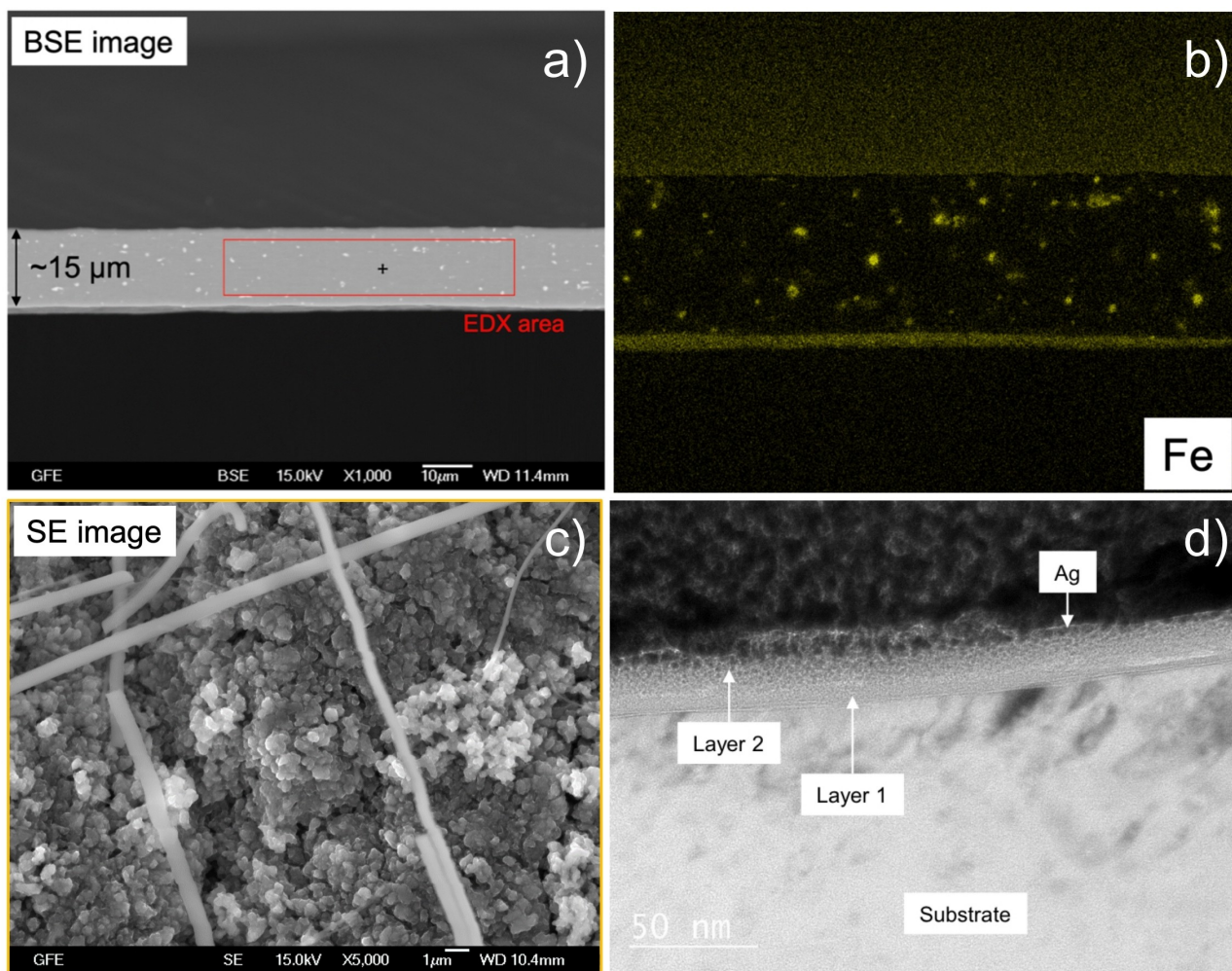
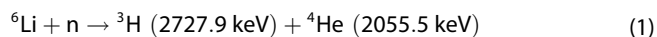


**Figure 1.** a) and b) Pristine aluminum foil displaying iron contamination throughout and on one surface. c) Nodular growth of amorphous aluminum oxides; suggested to be lithium aluminum oxide (Li–Al–O), and d) thicknesses of the native oxide layer “1” and ALD deposited layer “2”.

on the side free of iron. Figure 1d) displays the thickness and varied density throughout the cross section.

### Neutron Depth Profiling

Neutron depth profile experiments (NDP) were conducted on the TNDP spectrometer of the NPI CANAM infrastructure at the nuclear research reactor LVR15 in Řež (operated by the Research Center Řež). NDP, a non-destructive analytical technique for quantifying and measuring lithium that absorbs neutrons as a function of depth within the electrode material, is governed by the following nuclear reaction (Eq. (1))<sup>[18]</sup>



The method utilizes a nuclear reaction of Li atoms with neutrons, resulting in charged alpha ( $\alpha$ ) and triton (t) particles,  ${}^6\text{Li}(n,\alpha)t$  that exhibits a high cross-section of 940 barn. The sample irradiated by a thermal neutron beam is facing a solid-state detector and emitted charged particles with residual energies are counted with a multichannel analyzer. For each measurement performed, the spectrum was normalized by a neutron monitor measuring the fluence of neutron beam. Energy calibration was performed using isotopically enriched  ${}^6\text{LiF}$  sputtered on Mylar foil as standard. The t-

and  $\alpha$ -peaks in the raw NDP spectra were fitted with a Gaussian function to determine the peak positions and correlate them with the recoil energies of emitted particles from the  ${}^6\text{Li}(n,\alpha)t$  reaction in the samples. The calibration for elemental abundance was done by measuring an SRM2137 boron standard with a defined concentration of  $1.904 \pm 0.015 \times 10^{16} \text{ }^{10}\text{B}/\text{cm}^2$ , certified by the National Institute of Standards and Technology (NIST).

By comparing the peak areas in the NDP spectra with the Li concentration, it is possible to determine the scaling factor from counts to concentration. A methodology similar to that reported by Pivarnikova et al is employed in this study.<sup>[17]</sup> After calibration procedures, NDP was performed on aluminum foils with a 0%, 25% and 50% lithiation degree – with 100% state of charge (full lithiation) defined as the pure  $\beta$ -LiAl phase (Figure S1) – with a 2.8  $\mu\text{m}$  Kapton foil placed between the detector and sample to remove the  $\alpha$  contribution from the spectra and thus improve resolution of the triton contribution in bigger depths. The samples were measured in vacuum condition of about 1 mbar, from both sides to achieve the best depth resolution throughout the whole thickness of the foil. N4DP software was used to analyze and interpret the obtained data.<sup>[19]</sup>



## X-Ray Diffraction

Aluminum foil was electrochemically lithiated in half cells with a current rate of C/40 to a state of charge (SOC) of 25% and 50%. Hereby, the 100% state of charge (full lithiation) was defined as the  $\beta$ -LiAl phase. The electrodes were kept between two sheets of Kapton foil after the cell disassembly and during the measurement.

For the X-ray diffraction (XRD) measurements on the extracted aluminum foils, Empyrean X-ray diffractometer (Malvern Panalytical) was used with GaliPIX<sup>3D</sup> detector and MoK $\alpha_1$  radiation ( $\lambda = 0.70932 \text{ \AA}$ ). The samples were measured in transmission mode under rotation in a  $2\theta$ -range between  $7\text{--}49^\circ 2\theta$  with a step size of  $0.0035^\circ 2\theta$  and a measuring time of 42.59 s for each step. The total measuring time for each sample was between 7 and 36 h to ensure good statistics. One pristine aluminum foil as well as three aluminum foils at 25% and 50% lithiation degrees were probed. Furthermore, a LaB<sub>6</sub> NIST660c powder sample was measured as a reference sample. The phase analysis was conducted with HighScore<sup>[20]</sup> software.  $\alpha$ -LiAl,  $\beta$ -LiAl and LiOH phases were identified and used for the Rietveld refinement.

## Electrochemical Micro-Calorimetry

Heat flow data was collected by supplying current to coin cells housed in a TAM IV iso-thermal micro calorimeter (TA Instruments) in a  $40.00^\circ\text{C}$  environment. The cells were cycled using Keithley 2602 C sources. Currents were in the 1 mA range with an accuracy of  $\pm 0.02\% + 200 \text{ nA}$  with a 10 nA resolution. Voltages in the 6 V range are measured with an accuracy of  $\pm 0.015\% + 1 \text{ mV}$  with a  $10 \mu\text{V}$  resolution using a time resolution of less than 1 s. The samples were measured at a rate less than C/40 for fifteen consecutive cycles. The first lithiation was conducted at a rate of C/100 to avoid lithium plating while promoting the nucleation of the  $\beta$ -LiAl phase. The coin cells were sealed with epoxy to eliminate any noise from the heats of vaporization of electrolyte leaving the test samples. The detailed description of the equipment setup and methodology for these techniques is provided by Krause et al.<sup>[21]</sup> To ensure reproducibility, all electrical and thermal testing were conducted in triplicate and the error is represented by the standard deviation of the test group.

The coin cells were cycled in a capacity limited fashion to avoid the possible production of higher lithiated phases than  $\beta$ -LiAl and maintain mechanical robustness of the foil. This particular foil has been found to become mechanically unreliable past a lithiation degree of 60%. The first lithiation was performed at  $8.1 \text{ mA g}^{-1}$  (C/83) to avoid lithium plating while navigating the over-potentials associated with the first formation of  $\beta$ -LiAl. Subsequent delithiations and lithiations were conducted at  $16.3 \text{ mA g}^{-1}$  (C/40).

## 2. Results and Discussion

### 2.1. Neutron Depth Profiling and X-Ray Diffraction

NDP measurements are performed on aluminum foils with 0%, 25%, and 50% lithiation degrees. The raw NDP spectrum shows two strong triton (t) peaks around 2200 keV and 2700 keV, which stem from Li on the sample surfaces (Figure 2a)). The t particles lose energy as they move through the samples. Therefore, the peak at higher energy values results from Li accumulating near the top surface; and the t peak with lower energy is due to the reaction of neutrons with Li on the

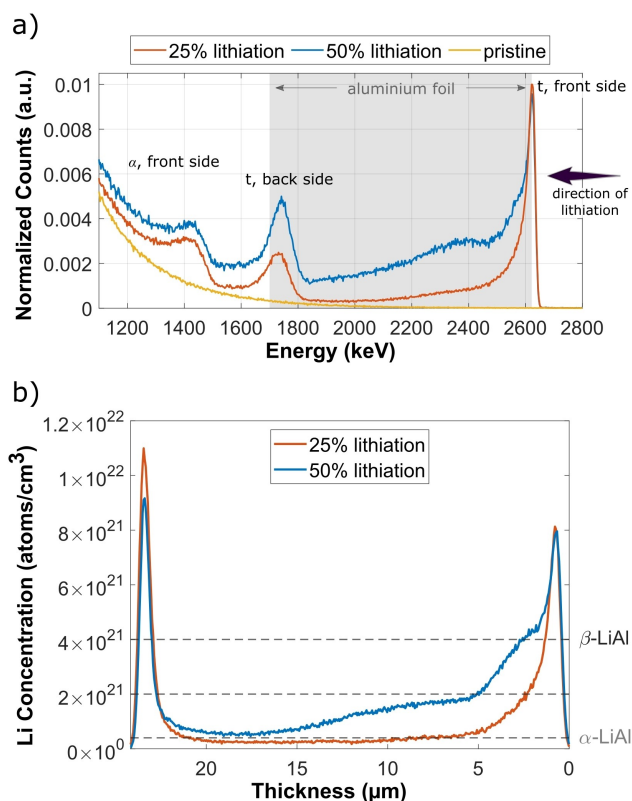


**Figure 2.** a) NDP spectra for 0%, 25% and 50% lithiation, and b) Combined Li depth profiles for the front side and back side measurements. The plateau of the 25% lithiated sample is assumed to be  $\alpha$ -LiAl phase with 5 at% Li, and thus the concentration of the  $\beta$ -phase is estimated using that value.

opposite (back) surface of the foil. The measured counts between these two peaks correspond to Li within the Al foil.

The onset of the  $\alpha$ -peaks, which contain the same information (with higher resolution but less penetration depth) as t, can be seen at lower energies where they are shifted due to the Kapton film used as a filter during the measurement. In contrast, the pristine Al foil has no notable peaks, which corresponds to no Li detection as was expected. The 25% and 50% lithiated samples show lithiation across the whole foil thickness, suggesting that no pristine aluminum zone is left inside the sample. Lithiated foils were measured from both sides to increase measurement accuracy. Here, the front side is defined as the side of the foil facing the separator during the lithiation, and the back side is the side facing the cell housing. The two measurements are combined at the point where the Li concentrations overlap (Figure 2b)).

For the NDP analyses, a uniform density of the foil is assumed, which corresponds to the density of pristine aluminum of  $\rho = 2.698 \text{ g/cm}^3$ , to estimate the thickness and the concentration. However, the actual density of the foil will be slightly lower since lithiated LiAl phases have lower densities than pure (non-lithiated) Al. For both foils, one can see high Li peaks at the surfaces on both sides, reaching up to about  $2 \mu\text{m}$  into the bulk of the foil. Liu et al. reported a substantial increase in Li concentration during operando measurements at the

interface between electrode and separator with a similar depth.<sup>[15]</sup>

On the front side, the surface peak has the same height for both lithiation degrees. In contrast, the back side shows a higher surface peak with a concentration of 25% lithiated foil exceeding the concentration of 50% lithiated foil. Since the surface peaks are visible on both sides, it is likely that during cell assembly, the electrolyte may have also infiltrated the back side of the Al foil.

Therefore, one can assume that the peaks partly result from either the formation of a solid-electrolyte interphase (SEI) or the formation of a Li–Al–O glass layer due to the electrochemical reduction of the native Al<sub>2</sub>O<sub>3</sub> in the presence of Li metal.<sup>[4]</sup> As a kinetic barrier for the formation of the crystalline  $\beta$ -LiAl needs to be overcome, it is also assumed that higher lithiated amorphous Li<sub>1+x</sub>Al phases are present at the surface.<sup>[22]</sup> This finding might explain why the surface peaks have the same concentration and width regardless of the lithiation degree. The peaks on the back side of the surface exhibit higher concentration values than the front side, which is somewhat surprising. It can be assumed that the Li on the front side will be extracted from that surface layer during lithiation and propagates towards the bulk region of the electrode. However, this remains the same at the backside as there is no such a driving force.

On the front side, the concentration of the 25% lithiated sample decreases monotonously towards the bulk of the foil. It is also visible that the concentration does not reach zero at any point, which confirms that the lithiation covers the whole thickness of the foil. For the 50% sample, the concentration shows a shoulder from 2–5  $\mu\text{m}$  with a higher slope before this slope declines again. From 5  $\mu\text{m}$  onwards, the concentration decreases at a slower rate, which is close to the 25% sample. However, the concentration does not reach the value of the 25% lithiation sample in the bulk of the foil and always remains at a higher level throughout the entire thickness.

Upon lithiation, aluminum forms a solid solution first with Li (Li<sub>x</sub>Al<sub>1-x</sub>,  $\alpha$ -LiAl) until it reaches the solubility limit (i.e., super-saturation stage) and then forms the  $\beta$ -LiAl phase after further lithiation.<sup>[23–25]</sup> In different studies, the solubility limit for Li inside aluminium is reported to lie somewhere between 5 at%<sup>[15,25]</sup> and 11 at% Li.<sup>[23]</sup> The transition from  $\alpha$ -LiAl to  $\beta$ -LiAl occurs at the surface when  $\beta$ -LiAl nuclei are formed that are growing vertically inside the bulk and protruding outwards.<sup>[1,9,15]</sup> For the 25% lithiated sample, the elevated Li concentration decrease from the surface towards the bulk indicates these  $\beta$ -LiAl regimes. Since the concentration inside the bulk is relatively constant, it can be assumed that it mainly consists of the  $\alpha$ -LiAl phase. For the 50% lithiated sample, the  $\beta$ -LiAl regimes grow further into the bulk, which is visible at elevated concentrations.

Since with NDP, the alpha and triton particles are detected only lose energy while passing through the material, 0  $\mu\text{m}$  depth corresponds to the actual surface of the foil regardless of surface roughness. The measured Li concentration gives the mean value throughout the sample area at that given depth. In the case of the formation of homogeneous lamellar-like  $\beta$ -LiAl with a clear edge between the  $\beta$ -LiAl phase and the less

lithiated  $\alpha$ -LiAl phase, which has been reported with SEM,<sup>[1,7]</sup> one would expect to see a clearly defined decay in the Li concentration at a distinct depth value in the NDP curve. As this is not the case, it can most likely be assumed to have a more inhomogeneous structure.

For the nucleation of the  $\beta$ -LiAl, an energy barrier must be surpassed.<sup>[26]</sup> This overpotential was suggested to originate from the necessary mechanical work for deforming the surrounding  $\alpha$ -LiAl phase.<sup>[27]</sup> Simultaneously, the overpotential affects the morphology of the  $\beta$ -LiAl as higher overpotentials result in faster nucleation rates and lead to a more homogeneous  $\beta$ -LiAl surface coverage.<sup>[1,9]</sup> In our case, the overpotential can be estimated to be around  $-0.1$  V, indicating the formation of ellipsoidal LiAl rather than homogeneous lamellar structures.

At 25% lithiation, it can be assumed that the structure of Al is not damaged too much, i.e. Al allows 25% of Li to be absorbed without a significant material disintegration, as this would cause a change in the Li depth profile otherwise. The visible shoulders for the 50% lithiated sample might originate from the inhomogeneities of the local  $\beta$ -LiAl particles at the given depth, which results in the gradual decrease of the concentration towards the bulk. Larger  $\beta$ -LiAl regimes are formed in the subsurface region up to 5  $\mu\text{m}$  depth due to the intensive lithiation process, and smaller regimes are formed at a depth of 5 to 17  $\mu\text{m}$ . Such structural inhomogeneities may be reflected in the double-slope Li profiles measured for the 50% lithiation sample. As the lithiation is not completed at either 25% or 50% degree of lithiation, not all the  $\beta$ -LiAl particles are expected to reach the back side of the Al foil. This is also visible in the concentration profile, where the concentration towards the back side is still significantly lower than the front (aside from the surface peaks). It is possible that the slopes detected for the 50% lithiated sample will even out after the lithiation is fully completed. If the concentration of the 25% lithiation sample in the bulk,  $c_0 \approx 4 \times 10^{20}$  Li/cm<sup>3</sup>, is assumed to be only  $\alpha$ -LiAl, one can calculate the expected concentrations for the  $\beta$ -LiAl phase (Figure 2b). For a solubility limit of 5 at% Li inside the  $\alpha$ -LiAl sample, the  $\beta$ -LiAl should have a Li concentration ten times (10x) that of the obtained value around  $c = 4 \times 10^{21}$  Li/cm<sup>3</sup>, which would correspond to the concentration around the 4  $\mu\text{m}$  mark for the 50% lithiation sample. Every concentration exceeding that value can also include even higher lithiated Li<sub>1+x</sub>Al or some surface components of the SEI, consisting of more than 50 at% Li.

Figure 3a illustrates the diffraction patterns for a pristine aluminum foil with lithiation degrees of 0%, 25% and 50%. Only aluminum can be identified in the diffraction pattern for the pristine sample. Lithiated samples show additional peaks that can be ascribed to  $\beta$ -LiAl (e.g.,  $2\theta = 11.10^\circ$ ), LiOH (e.g.,  $2\theta = 14.86^\circ$ ) and other phases, which are not visible in the pristine sample. The LiOH likely results from the reaction of Li with unavoidable traces of water in the electrolyte (i.e.,  $2\text{Li} + 2\text{H}_2\text{O} \rightarrow 2\text{LiOH} + \text{H}_2$ ). Since  $\alpha$ -LiAl has the same crystal structure with almost identical lattice parameters as pristine aluminum, it was impossible to fit both phases reliably using Rietveld refinement. However, NDP measurements suggest that all aluminum is partially lithiated. Thus, one can assume that only

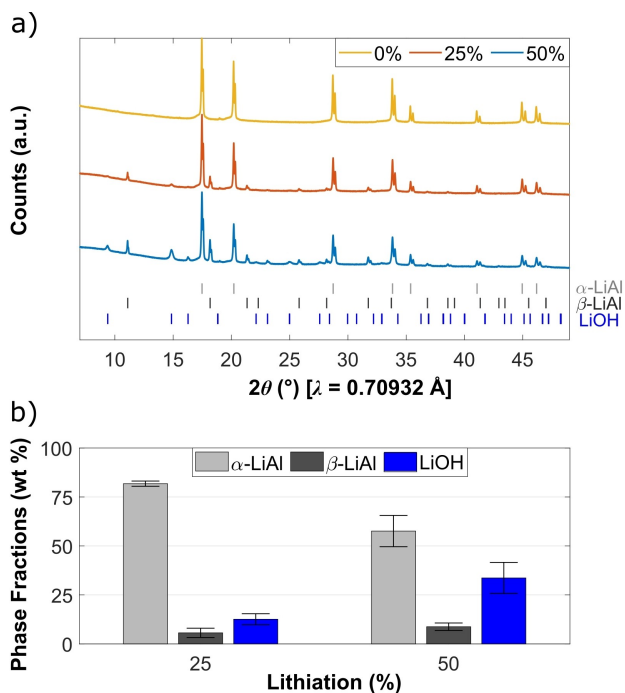


Figure 3. a) XRD patterns for different lithiation degrees (0%, 25% and 50%), and b) Phase fractions identified with Rietveld analysis for the 25% and 50% samples. Errors bars show standard deviations.

$\alpha$ -LiAl phase with increasing average Li content is present and can be used in the Rietveld Refinement. Furthermore, the aluminum/ $\alpha$ -LiAl peak intensities decrease with higher lithiation degrees. Higher lithiated crystalline phases could not be detected in any of the samples, which is in agreement with the phase diagram of LiAl.<sup>[26]</sup> The same goes for the metastable LiAl<sub>3</sub> phase.<sup>[28]</sup>

Quantitative phase analysis with Rietveld method was performed to determine the phase fractions. The data was fitted using the three phases, namely  $\alpha$ -LiAl,  $\beta$ -LiAl and LiOH, which yielded good results as depicted in Figure S2. From the phase analysis, the 25% lithiated samples contain higher amounts of  $\alpha$ -LiAl (Figure 3b), while the 50% lithiated samples have higher LiOH and  $\beta$ -LiAl amounts. Hereby, the difference in  $\beta$ -LiAl between the two lithiation degrees is relatively small, while the difference is more significant for LiOH. At 25% lithiation degree, the Li amount inside the foil should be around 12.5 at%. If the lithiation was uniform throughout the sample, one can expect to detect  $\alpha$ -LiAl almost exclusively inside the foil. As this is not the case, it can be reasonably concluded that an inhomogeneous lithiation pattern exists, forming a homogeneously lithiated  $\alpha$ -LiAl to some degree up to its solubility limit, before converting into  $\beta$ -LiAl. This mechanism is in agreement with the concentration profiles from the NDP data (Figure 2b). An increased accumulation of Li near the surface is visible, which decreases towards the bulk of the material.

The bulk's flatter concentration profile can be assigned to the  $\alpha$ -LiAl phase, whereas higher concentrations towards the surface might result from  $\beta$ -LiAl or higher lithiated phases. The relative ratio between  $\beta$ -LiAl and bulk  $\alpha$ -LiAl phase should

roughly be a factor of 4.5 to 10 (depending on whether the solubility limit for  $\alpha$ -LiAl is as low as 5 at% Li or as high as 11 at% as estimated from previous works).<sup>[15,23,25]</sup> NDP data from this study confirm that the solubility limit for  $\alpha$ -LiAl is closer to 5%.

The phase analysis shows that the amount of  $\beta$ -LiAl is slightly higher for the 50% lithiated sample, while the difference is more significant for LiOH. Therefore, it can be assumed that Li inside the  $\beta$ -LiAl phase can undergo reaction with the moisture (ca.  $2\text{Li} + 2\text{H}_2\text{O} \rightarrow 2\text{LiOH} + \text{H}_2$ ) and/or traces of oxygen that exist along with the moisture ( $\text{O}_2 + 2\text{H}_2\text{O} + 4\text{Li}^+ + 4\text{e}^- \rightarrow 4\text{LiOH}$ ) in ambient air or electrolyte to form the LiOH phase, a common degradation compound found on surfaces of electrodes.<sup>[29]</sup> This indicates that the surface peaks measured with NDP might also be attributed to the formation of LiOH. With the XRD, only crystalline phases inside the materials can be detected. Higher lithiated amorphous phases of aluminum like Li<sub>1+x</sub>Al might be present inside the foils since its growth has been detected before crossing the two-phase plateau in the potential curve.<sup>[22]</sup>

## 2.2. Electrochemical Micro-Calorimetry

The total energy loss arising from heat production/dissipation is mainly attributed to entropic ( $Q_{\text{entropic}}$ ), parasitic ( $Q_{\text{parasitic}}$ ) and polarization ( $Q_{\text{polarization}}$ , ohmic heat) factors. The parasitic factor refers to any chemical or electrochemical driven irreversible decomposition of electrolyte constituents (solvents, salt anions, additives, impurities), surface species, formation and decomposition of SEI layer, self-discharge etc. Figure 4 presents the voltage and thermal response during lithiation and delithiation processes as well as irreversible entropic changes during cycles 1 and 2.

The enthalpy potential,  $U_H$ , is expressed as in Equation (2).

$$U_H = U - \frac{\dot{q}}{i} \quad (2)$$

Where  $U$  is the cell potential (V),  $q$  is the thermal signal (W) and  $i$  is the current (A) response. The difference between  $U$  and  $U_H$  can be considered as entropy contribution. Immediately noticeable in this data (Figure 4 b) is that even with capacity limited cycling, the material drops below the  $\beta$ -LiAl plateau after the first cycle which has a coulombic efficiency greater than one; and this implies that the kinetics of delithiation is more the limiting factor than those involving the lithiation. During the first lithiation, it is also evident that the untreated (without Alumina coating) samples experience a linearly increasing enthalpy potential with the introduction of lithium. This is assumed to be from parasitic heating and is present in all untreated samples, while reduced (nearly invisible) in treated samples. However, it has to be noted that though the magnitude could be different, the possibility of having even lesser degree of parasitic heating on the treated samples cannot be neglected. Both the treated and untreated samples display lithiation beyond  $\beta$ -LiAl during the second cycle, which is not

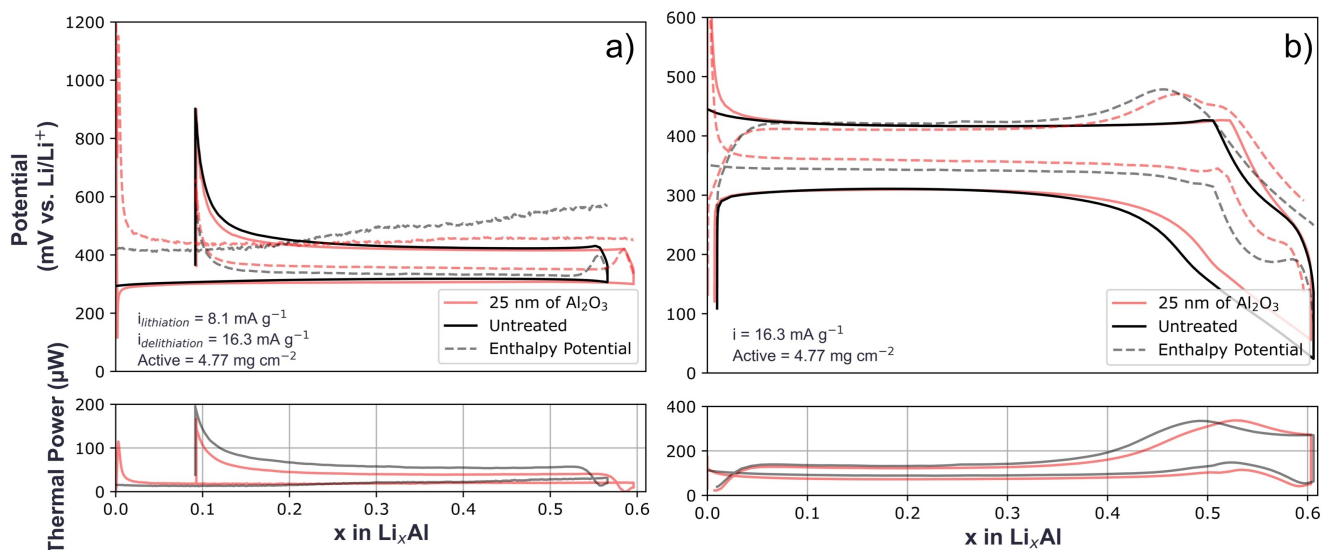


**Figure 4.** Electrical and thermal data from cycles: a) 1 and b) 2 of both untreated aluminum sample (black) and the sample with additional Al<sub>2</sub>O<sub>3</sub> deposited (red, treated). Dashed lines represent enthalpy potential while solid lines represent cell potential on the upper charts.

detected in the XRD analysis. During the first lithiation, the large overpotential associated with the nucleation of the  $\beta$ -LiAl phase is also apparent. This is shown in Figure 5a where the exotherm associated with the nucleation and initial formation of  $\beta$ -LiAl is measured. The addition of extra 25 nm of Al<sub>2</sub>O<sub>3</sub> (referred to as treated sample) is found to increase this energy by 63% (i.e., from 161 to 262 kJ mol<sup>-1</sup>).

The free energy associated with the formation of  $\beta$ -LiAl is calculated from the Nernst equation (Equation. 3) using the potential upon delithiation and is found to be 40.04 kJ mol<sup>-1</sup>. Figure 5b displays the enthalpy of formation while delithiating the  $\beta$ -LiAl phase where it is found to be 40.5 kJ mol<sup>-1</sup>, which is in a strong agreement with the calculated value.

This finding confirms that the nucleation energy barrier for the treated and untreated samples are 120.5 and 221.5 kJ mol<sup>-1</sup> respectively, as the measured heat during the initial generation of  $\beta$ -LiAl holds the heating from nucleation as well as the formation.

$$G = -nFE \quad (3)$$

Where G is the Gibbs free energy, n is the number of electrons transferred in the reaction, F is the Faraday constant (96.485 C/mol) and E is the potential difference.

Concerning the effect of alumina on the reversible lithiation of the material, it is clear from the coulombic efficiencies that it

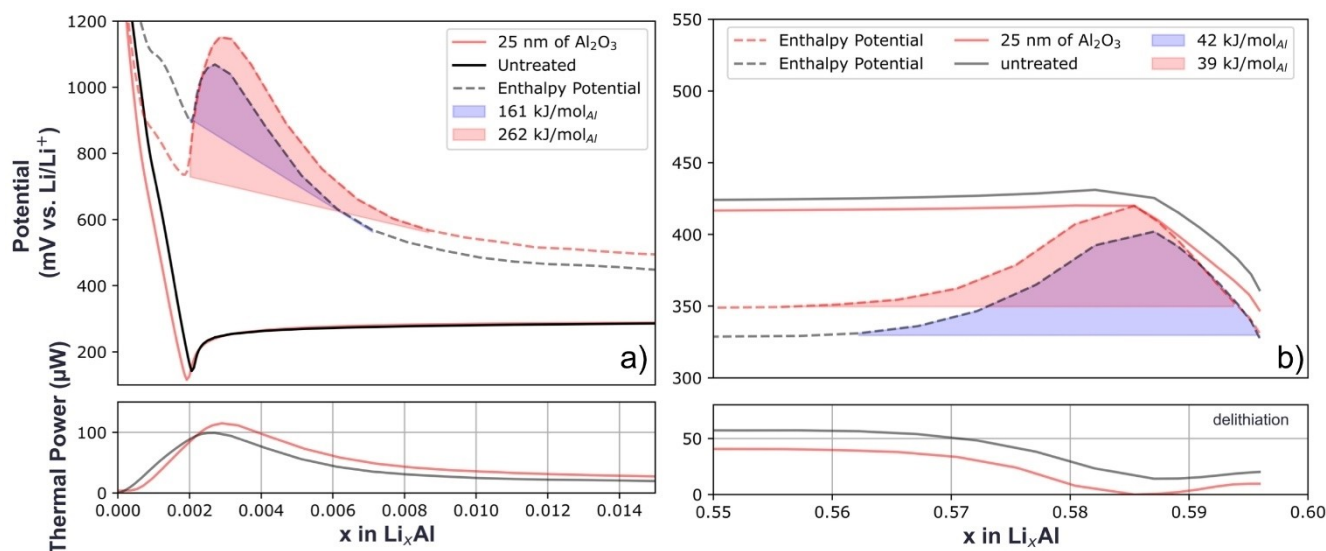


**Figure 5.** a) Electrical and thermal response during the first lithiation of both samples. The dashed line is the enthalpy potential. The integrals are the sum of the energy associated with the thermal event. b) Potential, heat flow, and enthalpy potential during the first delithiation displaying the enthalpy of formation for  $\beta$ -LiAl.



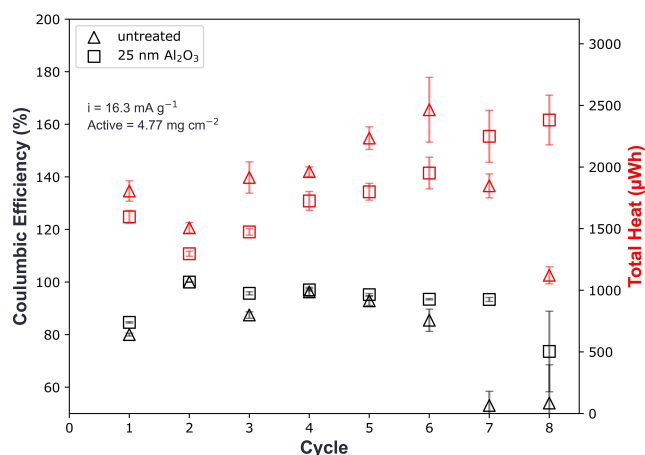


**Figure 6.** Coulombic efficiencies and total heat per cycle for treated (red) and untreated samples (black). The error represents the standard deviation of three cells.

does not have a negative impact (Figure 6). On average, throughout the life of both sample groups, the addition of 25 nm of Al<sub>2</sub>O<sub>3</sub> resulted in no statistically significant difference to the coulombic efficiencies, except in some aspects and (unexpectedly) a reduction in total heat production.

### 3. Conclusions

This work is aimed at investigating the role of alumina (Al<sub>2</sub>O<sub>3</sub>) in the nucleation and reversibility of  $\beta$ -LiAl. For this purpose, the reactivity of the native oxide (Al<sub>2</sub>O<sub>3</sub>) layer was monitored by introducing additional alumina and measuring the performance response from both electrical and thermal data. It is found that the 10x addition of alumina results in a significantly increased nucleation energy barrier compared to the untreated sample, yet no negative impact on the reversibility of the electrochemical response. The total heat measured during cycling is found to be reduced for the treated samples. Findings from this study suggest that the added Al<sub>2</sub>O<sub>3</sub> blocks the nucleation sites while fostering better passivation on the underlying aluminum. The enthalpy of formation for the  $\beta$ -LiAl phase is measured to be 40.5 kJ mol<sup>-1</sup>, in a strong agreement with the calculated value, 40.04 kJ mol<sup>-1</sup>, using Nernst equation. The nucleation energy barrier for aluminum with a native passivation layer was found to be 120.5 kJ mol<sup>-1</sup>. The coulombic efficiencies are also found to be slightly higher in the treated samples.

Furthermore, the lithiation of aluminum foil is found to be inhomogeneous as Li accumulates close to the interface between the electrode and separator, and decreases towards the bulk. NDP analysis evidenced the existence of two different slopes inside the aluminum foil, suggesting structural inhomogeneities. Further studies on the evolution of the Li distribution after consecutive cycles and the effect of different surface coatings on the reversibility of the lithiation process need to be conducted.

Lastly, calorimetry data obtained from this work strongly suggests that Al<sub>2</sub>O<sub>3</sub> does not play a role in the production of

Li–Al–O, which is one of multiple detrimental challenges plaguing the reversibility of aluminum anodes in lithium-ion batteries.

### 4. Supplementary Information (SI)

**Figure S1.** Electrochemical lithiation of the aluminium foils. 100% lithiation is defined as pure  $\beta$ -LiAl phase.

**Figure S2.** Rietveld refinement of a 25% lithiated Al foil. The identified phases are  $\alpha$ -LiAl,  $\beta$ -LiAl and LiOH.

### Acknowledgements

The authors acknowledge the German Federal Ministry of Education and Research (BMBF) for funding the project ExZellTUM III (03XP0255) within the ExcellBattMat cluster. Measurements were carried out at the CANAM infrastructure of the NPI CAS Rez. The employment of the CICRR infrastructure supported by MEYS project LM2023041 is acknowledged. Open Access funding enabled and organized by Projekt DEAL.

### Conflict of Interests

The authors declare no conflict of interest.

### Data Availability Statement

The data that support the findings of this study are available from the corresponding author upon reasonable request.

**Keywords:** aluminium · calorimetry · energy storage · lithium-ion battery · neutron depth profiling (NDP)

- [1] C. Trejo, K. Scanlan, A. Manthiram, *J. Electrochem. Soc.* **2024**, *171*, 40539.
- [2] a) M. N. Obrovac, V. L. Chevrier, *Chem. Rev.* **2014**, *114*, 11444; b) M. N. Obrovac, L. Christensen, *Electrochem. Solid-State Lett.* **2004**, *7*, A93.
- [3] a) E. C. Gay, D. R. Vissers, F. J. Martino, K. E. Anderson, *J. Electrochem. Soc.* **1976**, *123*, 1591; b) C. A. Melendres, C. C. Sy, *J. Electrochem. Soc.* **1978**, *125*, 727; c) B. M. L. Rao, R. W. Francis, H. A. Christopher, *J. Electrochem. Soc.* **1977**, *124*, 1490.
- [4] Y. Liu, N. S. Hudak, D. L. Huber, S. J. Limmer, J. P. Sullivan, J. Yu Huang, *Nano Lett.* **2011**, 4188.
- [5] a) A. S. Baranski, W. R. Fawcett, *J. Electrochem. Soc.* **1982**, *129*, 901; b) Y. Geronov, P. Zlatilova, G. Staikov, *J. Power Sources* **1984**, *12*, 155; c) T. R. Jow, C. C. Liang, *J. Electrochem. Soc.* **1982**, *129*, 1429.
- [6] a) D. Rehnlund, F. Lindgren, S. Böhme, T. Nordh, Y. Zou, J. Pettersson, U. Bexell, M. Boman, K. Edström, L. Nyholm, *Energy Environ. Sci.* **2017**, *10*, 1350; b) G. Oltean, C.-W. Tai, K. Edström, L. Nyholm, *J. Power Sources* **2014**, *269*, 266.
- [7] P. J. Crowley, K. P. Scanlan, A. Manthiram, *J. Power Sources* **2022**, *546*, 231973.
- [8] T. S. Huang, J. O. Brittain, *Mater. Sci. Eng.* **1987**, *93*, 93.
- [9] T. Zheng, D. Kramer, M. H. Tahmasebi, R. Mönig, S. T. Boles, *ChemSusChem* **2020**, *13*, 974.
- [10] T. Zheng, X. Wang, E. Jain, D. Kramer, R. Mönig, M. Seita, S. T. Boles, *Scr. Mater.* **2020**, *188*, 164.
- [11] T. Zheng, D. Kramer, M. H. Tahmasebi, R. Mönig, S. T. Boles, *ChemSusChem* **2020**, *13*, 5910.



- [12] T. Zheng, J. Zhang, X. Guo, W. Jin, S. T. Boles, *Electrochim. Acta* **2024**, *485*, 144127.
- [13] J. H. Park, C. Hudaya, A.-Y. Kim, D. K. Rhee, S. J. Yeo, W. Choi, P. J. Yoo, J. K. Lee, *Chem. Commun.* **2014**, *50*, 2837.
- [14] a) T. Chen, A. C. Thenuwara, W. Yao, S. E. Sandoval, C. Wang, D. H. Kang, D. Majumdar, R. Gopalaswamy, M. T. McDowell, *Batteries & Supercaps* **2023**, *6*; b) T. Zheng, D. Kramer, R. Mönig, S. T. Boles, *ACS Sustainable Chem. Eng.* **2022**, *10*, 3203; c) T. Zheng, S. T. Boles, *Prog. Energy* **2023**, *5*, 32001; d) X. Zhang, W. Zhao, J. Cai, C. Xu, S. Chen, G. Chen, G. Wang, *Solid State Ionics* **2022**, *387*, 116081; e) L. Yang, W. Zhao, S. Sun, C. Xu, H. Sun, X. Zhang, G. Wang, *Mater. Today Commun.* **2023**, *37*, 107179.
- [15] D. X. Liu, A. C. Co, *J. Am. Chem. Soc.* **2016**, *138*, 231–238.
- [16] a) F. Linsenmann, M. Trunk, P. Rapp, L. Werner, R. Gernhäuser, R. Gilles, B. Märkisch, Z. Révay, H. A. Gasteiger, *J. Electrochem. Soc.* **2020**, *167*, 100554; b) M. Wetjen, M. Trunk, L. Werner, H. A. Gasteiger, R. Gernhäuser, R. Gilles, B. Märkisch, Z. Révay, *J. Electrochem. Soc.* **2019**, *166*, A1408–A1411.
- [17] I. Pivarníková, M. Flügel, N. Paul, A. Cannavo, G. Ceccio, J. Vacík, P. Müller-Buschbaum, M. Wohlfahrt-Mehrens, R. Gilles, T. Waldmann, *J. Power Sources* **2024**, *594*, 233972.
- [18] a) G. Ceccio, A. Cannavó, J. Vacík, P. Horak, V. Hnatowicz, I. Tomandl, V. Lavrentiev, *J. Phys. Chem. C* **2020**, *124*, 25748; b) R. G. Downing, G. P. Lamaze, J. K. Langland, S. T. Hwang, *J. Res. Natl. Inst. Stand. Technol.* **1993**, *98*, 109.
- [19] M. Trunk, M. Wetjen, L. Werner, R. Gernhäuser, B. Märkisch, Z. Révay, H. A. Gasteiger, R. Gilles, *Mater. Charact.* **2018**, *146*, 127.
- [20] T. Degen, M. Sadki, E. Bron, U. König, G. Nénert, *Powder Diffr.* **2014**, *29*, S13–S18.
- [21] L. J. Krause, L. D. Jensen, J. R. Dahn, *J. Electrochem. Soc.* **2012**, *159*, A937–A943.
- [22] B. Qin, T. Diemant, H. Zhang, A. Hoefling, R. J. Behm, J. Tübke, A. Varzi, S. Passerini, *ChemSusChem* **2019**, *12*, 2609.
- [23] X. Zhu, M. Schoenitz, E. L. Dreizin, *J. Alloys Compd.* **2007**, *432*, 111.
- [24] Levine, E. D. Rapperport, E. J. Rapperport, *Trans. Metall. Soc. AIME* **1963**, *227*, 1204.
- [25] J. R. Owen, W. C. Maskell, B. C. H. Steele, T. Sten Nielsen, O. Toft Sørensen, *Solid State Ionics* **1984**, *13*, 329.
- [26] M. Z. Ghavidel, M. R. Kupsta, J. Le, E. Feygin, A. Espitia, M. D. Fleischauer, *J. Electrochem. Soc.* **2019**, *166*, A4034–A4040.
- [27] M. H. Tahmasebi, D. Kramer, R. Mönig, S. T. Boles, *J. Electrochem. Soc.* **2019**, *166*, A5001–A5007.
- [28] R. Sarmiento-Pérez, T. F. T. Cerqueira, I. Valencia-Jaime, M. Amsler, S. Goedecker, A. H. Romero, S. Botti, M. A. L. Marques, *J. Chem. Phys.* **2015**, *142*, 24710.
- [29] a) N. Akhtar, W. Akhtar, S. J. Wu, *Int. J. Cast Met. Res.* **2015**, *28*, 1; b) T. Furukawa, Y. Hirakawa, H. Kondo, T. Kanemura, E. Wakai, *Fusion Eng. Des.* **2015**, *98–99*, 2138.

---

Manuscript received: April 23, 2024

Revised manuscript received: May 31, 2024

Version of record online: July 31, 2024